RESEARCH ARTICLE
PLANETARY SCIENCES

Earth and Planetary Physics
10: 205–221, 2026
doi: 10.26464/epp2026005

Photometric modeling of ejecta for evaluating defensive Kinetic impacts on asteroids

XiaoYu Sun[1], ZhiJun Song[1], XiaoTao Guo[2], XiaoJing Zhang[3], Yuri Skorov[4], Yang Yu[1*], and He Zhang[5]

[1]Beihang University, Beijing 102206, China;

[2]State Key Laboratory for Space System Operation and Control, Xi'an 710043, China;

[3]China Academy of Aerospace System and Innovation, Beijing 102206, China;

[4]Max Planck Institute for Solar System Research, Göttingen 37077, Germany;

[5]China Academy of Space Technology, Beijing 100094, China

Key Points:

- We present a Monte Carlo photometric framework that couples ejecta sampling and dynamical evolution modeling to synthesize images that can be compared directly to HST, LICIACube, ground-based, and Lucy observations of the September 26, 2022, collision of the DART spacecraft with Dimorphos.
- Collision ejecta are decomposed into three components—a high-velocity (~1600 m/s) Na/K-bearing plume, low-velocity (~1 m/s) conical ejecta shaped by binary gravity and solar radiation pressure, and meter-scale boulders. Each component's mass and momentum contributions are separately quantified.
- Photometric decay curves and morphological evolution are fitted, to recover size–velocity distributions and, using scaling laws, to infer Dimorphos' bulk density, cratering parameters, and cohesive strength, thereby constraining momentum enhancement consistent with dynamical estimates.

Citation: Sun, X. Y., Song, Z. J., Guo, X. T., Zhang, X. J., Skorov, Y., Yu, Y., and Zhang, H. (2026). Photometric modeling of ejecta for evaluating defensive Kinetic impacts on asteroids. *Earth Planet. Phys.*, *10*(1), 205–221. http://doi.org/10.26464/epp2026005

Abstract: Kinetic impact is the most practical planetary-defense technique, with momentum-transfer efficiency central to deflection design. We present a Monte Carlo photometric framework that couples ejecta sampling, dynamical evolution, and image synthesis to compare directly with HST, LICIACube, ground-based and Lucy observations of the DART impact. Decomposing ejecta into (1) a high-velocity (~1600 m/s) plume exhibiting Na/K resonance, (2) a low-velocity (~1 m/s) conical component shaped by binary gravity and solar radiation pressure, and (3) meter-scale boulders, we quantify each component's mass and momentum. Fitting photometric decay curves and morphological evolution yields size–velocity distributions and, via scaling laws, estimates of Dimorphos' bulk density, cratering parameters, and cohesive strength that agree with dynamical constraints. Photometric ejecta modeling therefore provides a robust route to constrain momentum enhancement and target properties, improving predictive capability for kinetic-deflection missions.

Keywords: Kinetic impact; DART mission; ejecta dynamics; photometric modeling

1. Introduction

In this study, we employ NASA's Double Asteroid Redirection Test (DART) mission as a paradigm to demonstrate our photometry-driven ejecta modeling methodology. Kinetic impact has emerged as a leading strategy in planetary defense, with momentum transfer efficiency being a core parameter for mission design and performance assessment. Due to the substantial mass disparity between spacecraft and Earth-threatening asteroids, the resulting velocity change is expected typically to be on the order of millimeters per second for sub-kilometer-scale asteroids (Rumpf et al., 2017; Schmidt, 2019)—a minuscule fraction of their orbital speed, yet sufficient for long-term trajectory deflection. Conventional evaluation methods rely on long-term tracking of orbital displacement, usually requiring months or even years to detect meaningful position shifts. While extended observational baselines may theoretically enhance orbital determination accuracy, they also introduce significant dynamical uncertainties caused by Yarkovsky drift, planetary perturbations, solar tides, and radiation pressure (Capek et al., 2004; Hyland et al., 2010), which complicate momentum estimation.

First author: X. Y. Sun, 2629190958@qq.com
Correspondence to: Y. Yu, yu.yang@buaa.edu.cn
Received 30 JUN 2025; Accepted 08 SEP 2025.
First Published online 17 OCT 2025.

An alternative approach involves the physical and photometric characterization of impact ejecta. By analyzing the morphology, brightness, and kinematics of material expelled during an impact—captured through CubeSat, space telescopes, or ground-based observatories—it should be possible to constrain the ejecta mass, velocity distribution, and particle size. These constraints offer a more immediate and perturbation-resistant method for estimating the momentum transferred to a particular target body. Moreover, the ejecta behavior reflects the mechanical response of the impacted material, offering indirect access to the asteroid's bulk density, porosity, cohesion, and internal structure (Cheng B et al., 2023)—critical properties that remain difficult to determine through observation prior to the impact.

On September 26, 2022, the DART spacecraft collided with Dimorphos—the moonlet of the binary asteroid system Didymos—resulting in a measurable orbital period reduction of 33 ± 1 minutes and a momentum enhancement factor (β) estimated between 2.2 and 4.9, depending on the assumed bulk density of the target (Rivkin et al., 2021; Fahnestock EG et al., 2022; Cheng AF et al., 2023; Daly et al., 2023; Thomas et al., 2023; Chabot et al., 2024). These values imply that the momentum carried by the ejecta substantially exceeded that of the impactor, yet the distribution and origin of this ejecta-contributed momentum remain incompletely understood.

We present a hierarchical framework to resolve the momentum contributions from distinct ejecta components, including (1) a high-velocity plume (~1–4 km/s) dominated by resonance scattering from alkali atoms (e.g., Na, K) (Shestakova et al., 2023; Weaver et al., 2024); (2) a low-velocity conical ejecta (~1 m/s) forming complex structures under solar radiation pressure and binary gravity (Bagnulo et al., 2023; Opitom et al., 2023); and (3) meter-scale boulders, directly resolved in post-impact imagery (Jewitt et al., 2023; Farnham et al., 2023). In parallel, we apply a scaling-law-based inversion scheme to infer the physical properties of Dimorphos from observed photometric and morphological data. Specifically, we apply the point-source cratering model developed by Housen and Holsapple (2011) to parameterize the initial ejecta size–velocity distribution as a function of Dimorphos's bulk density, strength, and cratering parameters. These parameters are then constrained through comparisons with the observed photometric decay curves, morphological evolution, total estimated ejecta mass and momentum transfer.

The dynamical evolution and optical appearance of ejecta are fundamentally dependent on their initial conditions, particularly, the size–velocity distribution. Observations of the Didymos system—including orbital velocity and period change, ejecta morphology, total estimated ejecta mass, and the surface properties and shape of Dimorphos—have provided photometric, morphological, and dynamical constraints that led to a variety of impact scenario models and interpretations. Li JY et al. (2023), Deshapriya et al. (2023) and Dotto et al. (2024), constrained the geometry of the ejecta cone, including its axis orientation, opening angle, and elliptical cross-section. Cheng AF et al. (2020, 2022, 2024) conducted multiple rounds of impact modeling based on the point-source scaling laws of Housen and Holsapple (2011), refining the optical depth profile of the ejecta plume and constraining the material strength of Dimorphos to the range of 0–500 Pa. Raducan et al. (2024) employed smoothed particle hydrodynamics (SPH) simulations focusing on Dimorphos's rubble-pile structure, modeling only boulders larger than 2.5 m while treating the interstitial matrix as a loosely filled regolith. Their results, which prioritized constraints on momentum transfer, ejecta cone geometry, and total mass, suggest that Dimorphos likely has a bulk density below 2400 kg/m^3, with a relatively low volumetric fraction (≲40%) of boulders in its surface and shallow subsurface. Moreno et al. (2023) and Ferrari et al. (2022) developed an empirical power-law ejecta model that relates ejection speed to particle size, reproducing both the observed morphology and photometric profile of the tail.

However, current modeling approaches, typically based on single-regime formulations and focused on the slower, long-lived ejecta component, are unable to reconcile photometric constraints (e.g., brightness decay rate, morphology) with physical parameters (e.g., ejecta mass, momentum, and size distribution) across the full dynamical range of ejecta. To address these limitations, our framework separately resolves the dynamical properties of each ejecta regime, enabling a consistent integration of observational and physical constraints and allowing robust inference of Dimorphos's bulk properties.

Beyond the primary momentum imparted by the initial impact ejecta, other mechanisms of material ejection may also be present but are not considered in our momentum analysis due to their limited contribution. Specifically, secondary ejecta generated by particles reaccumulating onto the surface are expected to occur primarily on Didymos, and thus contribute little to the net recoil of Dimorphos. Seismic lofting caused by the propagation of impact-induced shockwaves through Dimorphos may eject regolith locally (Tancredi et al., 2023), but the resulting grains are likely to be small, approximately isotropic in their distribution, and low in total mass. As a result, neither mechanism is expected to meaningfully alter the net momentum budget in the direction of impact.

The remainder of this paper is organized as follows: Section 2 introduces the photometric datasets used in this work; Section 3 details our Monte Carlo-based modeling framework for ejecta sampling, orbital dynamics, and image synthesis; Section 4 presents the inversion of dynamical parameters and momentum decomposition; Section 5 describes the fitting of ejecta brightness to cratering models and the retrieval of physical parameters; Section 6 presents conclusions and discussion.

2. Multi-Instrument Observations and Photometric Analysis

At the time of impact, the Didymos system was located at a geocentric distance of 0.076 AU and a heliocentric distance of 1.05 AU, with a solar phase angle of 53.28° (Graykowski et al., 2023). Observations were conducted by a broad array of platforms, including ground-based telescopes, space-based observatories, the DART mission's companion CubeSat LICIACube, and NASA's deep-space mission Lucy. LICIACube performed a close flyby of Didymos approximately 167 seconds after impact, capturing images of the ejecta plume between 83 s and 243 s post-impact (Dotto et al., 2024). Concurrently, Earth-based facilities maintained long-term monitoring of the system over days to months, including the Hubble Space Telescope (Jewitt et al., 2023; Li JY et al., 2023), the 8-meter Very Large Telescope in Chile (Murphy et al., 2023;

Opitom et al., 2023), and various smaller observatories (Kareta et al., 2023; Lin ZY et al., 2023; Polishook et al., 2023; Lister et al., 2024; Moskovitz et al., 2024), along with amateur astronomers (Graykowski et al., 2023). The schematic illustration of the DART impact geometry is shown in Figure 1.

Graykowski et al. (2023) reported photometric measurements using a 13.6-arcsecond aperture (corresponding to ~750 km at the distance of Didymos), yielding a pre-impact apparent magnitude of m_V = 14.48 ± 0.11, and a post-impact peak brightness of m_V = 12.18 ± 0.03—an increase of 2.3 magnitudes, or a factor of ~8.32 in brightness. Kareta et al. (2023) compiled data from several ground-based telescopes using a 5″ photometric aperture (~276 km). Their analysis indicated that the system returned to pre-impact brightness between 24.3 and 25.3 days after impact. The brightness decay rate was 0.11–0.12 magnitudes per day in the first week, and 0.08–0.09 magnitudes per day over the entire monitoring period. These findings were supported by other independent datasets (Graykowski et al., 2023; Murphy et al., 2023). A temporary but distinct slowdown in brightness decay occurred between 5 and 8 days after impact, which Kareta et al. (2023) attributed to secondary ejecta generated by large boulders re-impacting the surface of Didymos. This interpretation is supported by direct observations of boulders within the ejecta plume (Jewitt et al., 2023).

Short-term photometric analyses revealed two distinct ejecta components in terms of velocity: a fast component averaging ~1.6 km/s and a slow component around ~1 m/s. Estimates of their contributions to the total post-impact brightness vary across different observations. Graykowski et al. (2023) reported 58% ± 2% from the fast ejecta and 42% ± 2% from the slow. Conversely, Weaver et al. (2024), using L'LORRI onboard Lucy, found 57.4% ± 2.2% from the slow component and 42.6% ± 2.3% from the fast.

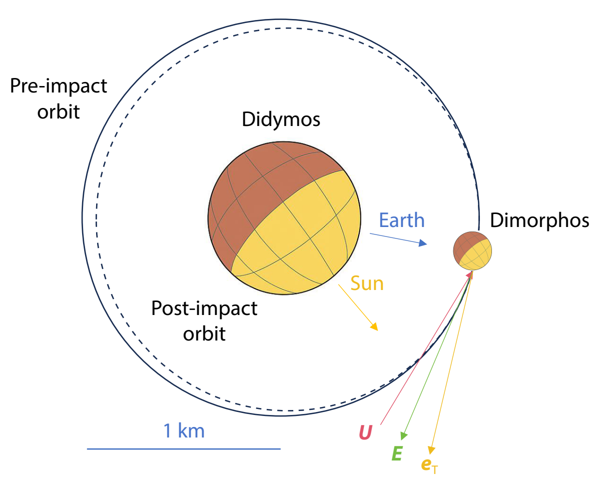

Figure 1. Schematic illustration of the DART impact geometry. The solid and dashed curves represent the pre-impact and post-impact orbits of Dimorphos around Didymos, respectively. The DART impact velocity (***U***), the net ejecta momentum vector (***E***), and Dimorphos's orbital velocity direction ($\boldsymbol{e}_T$) are indicated (Cheng AF et al., 2023). The direction of ***U*** is opposite to that of the other vectors, representing the actual impact direction (toward Dimorphos). The directions of the Sun and Earth relative to the system are also shown.

Despite such differences—possibly attributed to phase angle, viewing geometry, and instrument sensitivity—most studies agree that both components contribute comparably to the total optical brightness, emphasizing the importance of modeling the fast ejecta separately.

The fast ejecta exhibited velocities of ~1–4 km/s and appeared redder than the background (Graykowski et al., 2023; Murphy et al., 2023; Dotto et al., 2024). Ofek et al. (2023) initially attributed this to Mie scattering by submicron particles, but subsequent modeling indicated that such a mechanism would require an unphysical ejecta mass (~9000 kg), exceeding energy constraints. Shestakova (2023) identified strong Na, K, and Li resonance lines in this component and suggested that its brightness arose predominantly from resonant scattering by alkali atoms, particularly the sodium D-line at 589 nm. Dust scattering was likely a minor contributor, but the precise ratio remains unclear.

The slow ejecta, with an average velocity of ~1 m/s, underwent complex orbital evolution influenced by binary gravity and solar radiation pressure. It gave rise to the main photometric structures observed 0–25 days after impact, including a broad ejecta cone (opening angle: 125° ± 10°), an anti-solar dust tail, and a secondary tail located ~4° north of the main tail between days 5–8 (Li JY et al., 2023; Moreno et al., 2023). LICIACube images showed filamentary and clumpy features within the cone (Dotto et al., 2024). The cone was formed by large, relatively fast particles that escaped the binary gravity early, maintaining a conical geometry with minimal influence from radiation pressure. By contrast, the anti-solar tail consisted of smaller, slower particles that were rapidly accelerated away, forming a size-sorted trail. Li JY et al. (2023) linked the tail's brightness profile to particle size distribution, deriving a broken power-law with slopes of −2.7 ± 0.2 for 2 μm–6 mm and −3.7 ± 0.2 for particles larger than 6 mm. Moreno et al. (2023) independently confirmed the steeper slope, though their analysis was constrained to <6 cm, beyond which the particle statistics became too sparse for reliable slope determination.

The origin of the secondary tail remains uncertain. Li JY et al. (2023) proposed that it may have been caused by ejecta re-impacting the binary surfaces, consistent with the 5–8 day brightness plateau observed by Kareta et al. (2023). Other potential mechanisms include interactions between the slow-moving ejecta and the binary gravitational field (Moreno et al., 2022), gravitational deflection of returning dust grains under solar radiation pressure (Ferrari et al., 2022), or the motion of photoionized dust influenced by the interplanetary magnetic field (Hartzell, 2019). Such ambiguities in the physical origin of the secondary tail highlight the need for direct observational constraints. ESA's Hera mission, arriving at the Didymos system in late 2026, is expected to play a critical role in resolving these uncertainties (Michel et al., 2022). By conducting in situ measurements, Hera will provide high-fidelity estimates of the system's mass distribution and bulk density, significantly improving the precision of orbital modeling for re-impacting or gravitationally-deflected ejecta. In addition, high-resolution imaging of both Didymos and Dimorphos will enable detailed shape reconstructions after impact, allowing for more accurate estimates of the total ejected mass. Surface imaging may also reveal the spatial distribution of secondary craters, offering insights into the extent and nature of possible secondary impacts. Furthermore, if any ejecta material remains gravitationally bound at the time of Hera's arrival, the mission may directly characterize its physical properties, including particle size distribution, porosity, and electrostatic behavior, thereby shedding new light on the post-impact evolution of the system.

Several months after the impact, most ejecta had dispersed. Jewitt et al. (2023) identified 37 slow-moving point sources in HST images, interpreted as meter-scale boulders ejected during the impact. The largest boulder had a diameter of ~7 m (assuming albedo = 0.15). Based on their projected motions in the plane of the sky, the average speed was estimated to be 0.30 ± 0.03 m/s—slightly above the escape velocity of the Didymos system (~0.24 m/s). Interestingly, Farnham et al. (2023) also reported isolated bright spots in LICIACube's flyby images taken ~167 s after impact, which may represent similar large fragments, though they have yet to be analyzed in detail. These multi-source observational constraints form the basis of our momentum transfer modeling, presented in Section 4.

3. Methods

This section outlines our numerical framework for modeling the DART impact ejecta and generating synthetic observations. We employ established cratering scaling laws to characterize the ejecta (see Supplementary Materials for detailed formulation) and a tailored sampling strategy to mimic the ejecta size distribution. We perform dynamical simulations of the ejecta's ballistic motions based on estimates of gravitational and radiative forces. Using radiative transfer modeling, we synthesize images of the modeled ejecta, enabling direct comparison with telescopic and spacecraft image data.

3.1 Sampling Strategy for Monte Carlo Simulation

At asteroid scale, the number density of ejecta particles commonly follows a power-law size distribution. This is expressed by:

$$N(d) = N_0 d^q, \ d_{min} \le d \le d_{max}, \tag{1}$$

where q is the power-law index, d_{min} and d_{max} are the minimum and maximum particle sizes within the range, and N_0 is a normalization factor determined by the total ejecta mass. The power-law indices q used here (−2.7 ± 0.2 for 2 μm–6 mm and −3.7 ± 0.2 above 6 mm) were introduced in Section 2 based on Li JY et al. (2023) and Moreno et al. (2023). The theoretical cumulative particle-size distribution derived from this power law is shown by the thick black dashed "Theoretical Distribution" curve in Figure 2.

In practical computation, this continuous distribution must be discretized into N_s sampled particles. Each sampled particle represents a cluster of real particles with similar size and velocity; the sampling ratio is defined as the number of real particles represented by each sampled one. To ensure adequate statistical resolution and to preserve the continuity of the underlying distribution, we adopt $N_s \ge 10^7$ for each ejecta component. The total number of particles was chosen based on a balance between statistical precision, physical representativeness, and computational feasibility. Our size distribution spans seven orders of magnitude (from microns to meters), so a sufficiently large sample in each size decade is required to guarantee statistically meaningful coverage across the entire size range. Similar studies of asteroid ejecta dynamics (e.g., Yu Y et al., 2017; Fahnestock et al., 2022; Moreno et al., 2023) employ 10^6–10^8 particles. Our own parallelized C++ code completes a 10^7-particle run in a few hours on multi-core hardware; To increase our N_s by another order of magnitude would dramatically extend run times and impede systematic parameter exploration, hence we have chosen N_s ~10^7 to be an optimal trade-off at this time.

We performed inverse transform sampling: first, N_s random numbers are uniformly drawn within the size interval to generate a set of samples d. A transformation function $d = g(s)$ is then constructed such that the transformed variable s follows the desired power-law distribution. The transformation function is

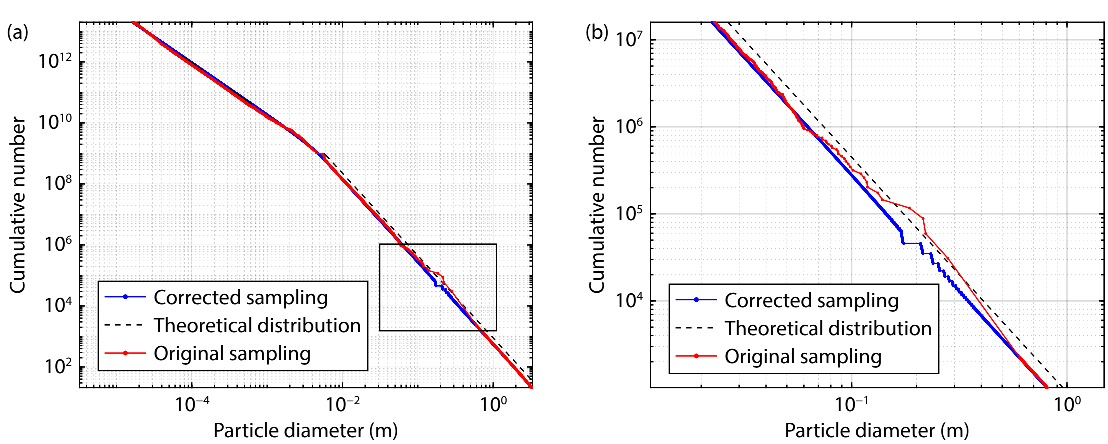

Figure 2. Cumulative particle size distributions obtained from different sampling strategies. The *x*-axis represents particle diameter (in meters), while the *y*-axis indicates the cumulative number of particles larger than a given diameter. In panel (a), the red line shows the result of inverse transform sampling applied segment-wise across the size distribution; the black dashed line represents the expected theoretical distribution; the blue line illustrates the outcome of the corrected sampling method proposed in this study. Panel (b) presents a magnified view of the region outlined by the black box in (a), highlighting finer differences among the sampling methods.

$$s = g^{-1}(d) = \left[\frac{d - d_{\min}}{d_{\max} - d_{\min}}\left(d_{\max}^{q+1} - d_{\min}^{q+1}\right) + d_{\min}^{q+1}\right]^{\frac{1}{q+1}}. \quad (2)$$

This sampling method theoretically reproduces the target power-law distribution. However, in practice, the broad range of particle sizes—from microns to meters—introduces statistical imbalance. Large particles, though few in number, may be under-sampled, reducing their representation in synthetic images and potentially influencing momentum predictions. For example, if we were to sample across the entire 1 μm–1 m size range strictly in proportion to the true population ratio (e.g. 10^{11} real particles to 10^{7} sampled particles), the expected number of samples in the 1 mm–1 m interval would be below one. This obviously results in severe under-sampling of the large-particle regime. A straightforward remedy might be to divide the size range into finer bins, increasing the resolution in the large-particle regime. However, this approach risks overrepresenting rare large particles and may introduce artificial discontinuities at bin edges. In our model here, we split 2 μm–2 m into 2 μm–60 μm, 60 μm–6 mm, 6 mm–0.6 m, and 0.6 m–2 m with on the order of 10^{6} samples per bin, as illustrated by the red dotted "Original Sampling" curve in Figure 2; this approach creates a pronounced sampling gap in the 0.1 m–0.6 m interval. This sampling gap translates directly into our synthetic imaging, producing a noticeable drop in brightness for particles in that size range that results in an artificial planar discontinuity in features such as the antisolar tail, thereby reducing image fidelity. To address this, we adopt a hybrid sampling strategy that separately treats small and large particles. Large particles are deterministically sampled (sampling ratio = 1) to ensure complete representation, while small particles continue to be generated probabilistically using inverse transform sampling. Concretely, we divide the full size range into w uniform bins (e.g., each bin's width is 1μm):

$$d_i = d_{\min} + \left(\frac{i}{w}\right)(d_{\max} - d_{\min}),\ \ i = 0,1,\ldots,w. \quad (3)$$

Starting from the largest size bin (i.e., most sparsely populated), we search downward until the expected particle count in a bin reaches 1—this particle size is then taken as the boundary between large and small particles. In our model, this cutoff occurs at approximately 0.17 m. All particles in the large-size regime are sampled completely, with each sampled particle representing a single physical particle. The remaining smaller particles are sampled using inverse transform sampling based on Equation (3), with sampling ratios determined by the desired total count, as illustrated by the blue dotted "Corrected Sampling" curve in Figure 2.

The original and modified sampling methods are compared in Figure 2. To evaluate the continuity of our particle sampling strategy across the broad size range, we introduce three complementary indicators: the Normalized Maximum Gap $G_{\max}$, the Mean Inter-Particle Gap $\bar{g}$, and the Coefficient of Variation of Gaps CV_g, all defined in logarithmic diameter space.

We let the diameters of the sampled particles be d_i (in meters), and define the corresponding logarithmic values as $x_i = \log_{10} d_i$, where $i = 1, 2, \ldots, N_s$ and $x_1 \le x_2 \le \cdots \le x_{N_s}$. We define the adjacent spacing (log-scale gaps) as

$$g_i = x_{i+1} - x_i,\ \ i = 1,2,\ldots,N_s - 1. \quad (4)$$

The Coefficient of Variation of Gaps is calculated by Equation (5), where $\bar{g}$ is the average of g_i:

$$CV_g = \frac{\sqrt{\frac{1}{N_s - 1}\sum_{i=1}^{N_s-1} g_i}}{\bar{g}}. \quad (5)$$

These metrics reflect how evenly the sampled particle sizes are distributed: smaller values indicate a more continuous and homogeneous sampling; larger values reveal clustering or voids. Such continuity is especially critical in our model, as the synthetic brightness images ultimately rely on smooth representation of ejecta across all size scales. Gaps in the sampled diameter range would translate into brightness discontinuities in image simulations, particularly in the formation of tail structures or brightness gradients. As shown in the comparison Table 1, below, the revised sampling strategy significantly improves all three metrics compared to the initial approach.

These results confirm that the corrected sampling method better captures the continuous nature of the theoretical size distribution, thereby ensuring a more physically realistic and visually coherent synthetic image. By improving balanced sampling across the entire size range, this refinement reduces the likelihood of artificial brightness discontinuities in the simulated ejecta morphology.

3.2 Mechanical Environment of the Ejecta Propagation

In this section, we analyze the various forces acting on ejecta particles in the context of a binary asteroid system, and incorporate known observational constraints on the Didymos system's physical parameters.

Several physical and dynamical properties of the Didymos system have been well characterized through ground-based and spacecraft observations (Michel et al., 2016). In this study, we adopt the polyhedral shape models of Didymos and Dimorphos, constructed from photometric observations (Pravec et al., 2022), to simulate particle-surface interactions within the binary system. The impact geometry, including the spacecraft configuration, impact site, and angle of incidence, is also well established. Table 2 summarizes the adopted parameters for our numerical modeling, all of which are mutually supported by independent studies (Naidu et al., 2015; Cheng AF et al., 2023; Daly et al., 2024; Raducan et al., 2024; Richardson et al., 2024).

Table 1. Continuity metrics used to evaluate the smoothness of particle size sampling.

Method	Normalized Max Gap	Mean Gap	Coefficient of Variation
Original sampling	0.1042	0.000082	30.3404
Corrected sampling	0.0119	0.000038	8.6506

Table 2. Physical and dynamical parameters of 65803 Didymos system and DART incident[a].

Parameter	Value	Reference
Didymos dimensions (m)	851 × 849 × 620	Cheng AF et al., 2023
Didymos grain density (kg/m^3)	3400	Richardson et al., 2024
Didymos bulk density (kg/m^3)	2700	Richardson et al., 2024 Naidu et al., 2015
Dimorphos dimensions (m)	177 × 174 × 116	Raducan et al., 2024 Daly et al., 2024
Dimorphos grain density (kg/m^3)	3400	Richardson et al., 2024
Dimorphos bulk density (kg/m^3)	1500–3400	Cheng AF et al., 2023 Richardson et al., 2024
Dimorphos cohesive strength (Pa)	5–500	Richardson et al., 2024 Raducan et al., 2024
DART impactor mass (kg)		
DART impactor velocity (km/s)	579.4	Cheng AF et al., 2023
Ejecta cone direction		
Pre-impact orbit separation (km)	1.206	Cheng AF et al., 2023 Naidu et al., 2015
Pre-impact orbit period (h)	11.9215	Cheng AF et al., 2023 Naidu et al., 2015

[a]Direction vectors are defined in the EME J2000 coordinate frame.

The physical processes influencing ejecta motion are grouped into three categories (Yu Y et al., 2017; Li XY et al., 2023; Wijayatunga et al., 2023; Burattini et al., 2024): (1) Collisions between particles and with the binary components; (2) Gravitational forces from the binary, the Sun, and other celestial bodies; (3) Radiative forces, including solar radiation pressure (SRP) and the Yarkovsky effect.

These contributions are considered as follows:
During the initial excavation phase (within the first few minutes post-impact), particle collisions are frequent and significantly influence the ejecta dynamics. However, this stage is modeled using empirical point-source cratering scaling laws, which effectively encapsulate the collective effects of particle–particle interactions. As the ejecta cloud expands and enters the ballistic transport phase, collisions become increasingly rare and have negligible impact on the net momentum imparted to Dimorphos. Therefore, inter-particle collisions are not explicitly modeled in the subsequent dynamical simulations.

Gravitational and radiative forces dominate the subsequent evolution of the ejecta, with their relative importance depending on both the particle size and its distance from the asteroid. We approximate the dominant gravities from Didymos and Dimorphos using point masses. While non-spherical gravity becomes relevant for slow-moving particles near the surface, this effect is neglected here; our analysis focuses on faster-moving fragments that quickly escape the binary's gravitational influence and contribute the majority of the momentum transfer. Solar gravity, the most significant external perturbation apart from the binary's own gravity, is computed using high-precision ephemerides from the JPL Horizons system.

Solar radiation pressure (SRP) is modeled via the parameter $\alpha_{\rm SRP}$, defined as the ratio of radiation pressure to solar gravity (Burns et al., 1979). Although the actual radiation pressure experienced by a particle depends on its size, shape, material composition, and surface optical properties, this approximation is widely used and has been shown to provide sufficiently accurate results for micron- to millimeter-sized grains under solar illumination. Given that our focus is on the large-scale motion and brightness evolution of the ejecta cloud rather than detailed radiative transfer, the current formulation of SRP is both appropriate and consistent with standard practice in similar studies:

$$\alpha_{\rm SRP}=\frac{3\epsilon S_{\rm sun}r_0^2}{2cGM_{\rm sun}\rho_{\rm s}d}, \tag{6}$$

where $S_{\rm sun}$ is the solar constant at 1 AU (~1.36 × 10^3 W/m^2; Kopp and Lean, 2011), ϵ is the particle reflectivity (1 for total absorption, 2 for total reflection), d is particle diameter, $\rho_{\rm s}$ is particle density, c is the speed of light in vacuum (~2.9979 × 10^8 m/s), $GM_{\rm sun}$ is the solar (heliocentric) standard gravitational parameter (~1.3271244 × 10^{20} m^3/s^2), r_0 is the reference heliocentric distance defined as 1 AU, and AU denotes the astronomical unit (1 AU = 149,597,870,700 m). The $\alpha_{\rm SRP}$ factor is inversely proportional to particle size. SRP becomes the dominant acceleration for particles smaller than 100 μm, which are quickly swept out of the system. We incorporate, also, a shadowing mechanism: SRP is temporarily nullified when particles enter the shadow cast by the asteroid. The Yarkovsky force and planetary perturbations are negligible on the timescale of one month and are thus neglected.

Particle trajectories are computed using a restricted three-body problem solver developed by Yu Y et al. (2017), with an adaptive step-size Fehlberg 7(8) Runge–Kutta integrator (Fehlberg, 1969). The solver, written in parallelized C++, assumes spherical particles and uses the polyhedral model of Didymos to calculate collisions and shadowing. At each time step, our code checks for surface impacts. Once a particle contacts the asteroid surface, it is assumed to stick and is removed from further computation. The position and velocity of each particle can be out-put at any specified time, enabling the generation of synthetic images, momentum analysis, and comparisons with observed morphological features.

3.3 Photometry-based Imaging Synthesis

In this section, we describe our method for converting the spatiotemporal distribution of ejecta into synthetic images comparable to those observed from Earth or space-based instruments. The imaging model simulates a central-projection CCD optical camera, detecting sunlight scattered toward the camera's focal plane by ejecta components. The heliocentric ecliptic coordinate system is denoted $O{-}X_rY_rZ_r$, the camera-centered space coordinate system is $S{-}X_xY_xZ_x$, and the image plane coordinate system is $o{-}x_py_p$. The camera center has coordinates (X_{rS}, Y_{rS}, Z_{rS}) in the heliocentric frame, and the projection of a point appears at $(x_x, y_x, -f)$ in the image-space frame, where f is the focal length. Based on photogrammetric principles, the object point, projection center, and image point are collinear, satisfying the collinearity Equation (7):

$$\begin{cases} x_x = -f\dfrac{a_{11}(X_r - X_{rS}) + a_{12}(Y_r - Y_{rS}) + a_{13}(Z_r - Z_{rS})}{a_{31}(X_r - X_{rS}) + a_{32}(Y_r - Y_{rS}) + a_{33}(Z_r - Z_{rS})}, \\ y_x = -f\dfrac{a_{21}(X_r - X_{rS}) + a_{22}(Y_r - Y_{rS}) + a_{23}(Z_r - Z_{rS})}{a_{31}(X_r - X_{rS}) + a_{32}(Y_r - Y_{rS}) + a_{33}(Z_r - Z_{rS})}. \end{cases} \tag{7}$$

The coefficients a_{ij} in the collinearity equations represent the elements of the rotation matrix $\boldsymbol{R}$, which defines the orientation of the camera frame $S{-}X_xY_xZ_x$ with respect to the heliocentric coordinate system $O{-}X_rY_rZ_r$.

Scattering behavior of the particles is modeled using a constant-phase scattering model derived from DART ejecta studies (Lolachi et al., 2023). The phase function $F_{11}(\alpha)$, where α is the phase angle, is defined as:

$$F_{11}(\alpha) = F_{11}(0)\,10^{-0.4C_P\alpha}, \tag{8}$$

where C_P is the linear phase coefficient, and $F_{11}(\alpha)/4\pi$ gives the directional scattering probability. The apparent magnitude m_p of a particle is calculated via radiative transfer as follows (Moreno, 2023):

$$p_R\pi r^2 = \frac{\pi r_h^2\Delta^2 10^{0.4(m_{\rm sun}-m_p)}}{r_0^2 G(\alpha)}, \tag{9}$$

where r_h and Δ are the heliocentric and geocentric distances of the asteroid (in meters), $m_{\rm sun}$ is the solar apparent magnitude in the given band, p_R is the geometric albedo at zero phase angle, and $G(\alpha) = 10^{-0.4C_P\alpha}$ is the phase correction.

Under the spatial and temporal scales relevant to ground-based observations (up to ~25 days), the ejecta cloud is assumed to be optically thin—meaning no mutual shadowing occurs. The total brightness in each image pixel is the sum of contributions from all particles within the corresponding solid angle. Based on our calculations, the spatial number density of ejecta remains sufficiently low to satisfy the optically thin condition throughout the time frame of interest (from ~30 minutes to ~25 days post-impact). Therefore, Equation (9) can be directly applied to estimate the projected brightness distribution.

Noise sources such as background flux, photon shot noise, and CCD dark current introduce uncertainties into the simulation. These effects are especially significant in the late-stage evolution of the ejecta cloud, when small particles have been dispersed by SRP and only sparse cm- to dm-sized particles remain, producing weak signals that may fall below detection thresholds. For simplicity, we set a limiting magnitude of 30, and disregard pixels whose total brightness falls below this level. A more precise modeling approach would involve signal-to-noise analysis for specific instruments, accounting for zodiacal and galactic background light, readout noise, thermal noise, and dark current, as well as telescope aperture, quantum efficiency, exposure time, and atmospheric extinction for ground-based setups, all of which are beyond the scope of this work.

4. Analysis on the Composition and Transfer of the Momentum

Based on the observed change in the binary system's orbital period, Dimorphos experienced a reduction of 2.70 ± 0.10 mm/s in its orbital velocity component along the direction of motion due to the DART impact. For a bulk density range of 1500–3300 kg/m³, the inferred momentum enhancement factor β varies linearly from 2.2 to 4.9 (Cheng AF et al., 2023). In this study, we decompose the total ejecta momentum into three distinct components: fast ejecta, sub-meter slow ejecta, and meter-scale boulders. The rationale for modeling the fast and slow ejecta components separately has been established in previous sections. Meter-scale boulders are treated independently as they carry a lot of mass but contribute very little to the brightness, and their velocities and sizes can be directly inferred from HST observations, enabling more accurate momentum estimates.

We assume that the ejecta curtain is axisymmetric about the impact momentum vector and neglect heterogeneity introduced by surface features. Although localized concentrations such as streaks and clumps have been reported (Dotto et al., 2024) and may explain the filamentary structures observed by Li JY et al. (2023), our focus is on the net ejecta momentum rather than its detailed morphology. Under this assumption, we consider the total ejecta momentum to be aligned with the impact momentum (previous studies suggest a deviation angle of only ~5°). Our model also assumes instantaneous ejection and momentum transfer, justified by the fact that the cratering and ejecta launch processes are expected to be complete within several hundred milliseconds—negligible compared to the dynamical timescale of the system (Hoerth et al., 2013). Minor torques resulting from the slightly off-center impact are neglected, as they are insignificant compared to the overall angular momentum change of Dimorphos. Effects such as reshaping or mass loss are also ignored, as their magnitude is below the current uncertainty in the orbital period measurements (Cheng AF et al., 2023).

4.1 The Fast Ejecta

The fast ejecta rapidly exited the photometric apertures of most instruments within minutes after impact (Graykowski et al., 2023; Weaver et al., 2024), experiencing negligible influence from solar radiation pressure and gravitational forces. Their motion can therefore be approximated as uniform linear trajectories in the image plane. Given that the Earth-based viewing geometry was nearly perpendicular to the impact momentum vector (see Figure 1), the observed projected velocities closely reflect the true ejection speeds.

The total brightness within the 13.6-arcsecond (750 km) aperture is assumed to be proportional to the integrated scattering cross-section of particles within the field of view. As the fast ejecta leave the aperture, the measured brightness declines accordingly. By analyzing the rate of brightness decay at successive time steps, we can obtain the instantaneous mass of ejecta exiting the aperture. Since the particles are approximated to follow straight-line motion, the timing of their departure can be translated into projected velocity. Applying this method, we find that fast ejecta exited the aperture between 184 s and 780 s post-impact, with projected velocities ranging from 1 to 4 km/s. The peak of the brightness curve corresponds to an average projected velocity of 1.9 ± 0.2 km/s. The photometric observations from Graykowski et al. (2023), used to derive the velocity–mass distribution, are shown in Figure 3a.

As we discussed in Section 2, the observed brightness of fast ejecta includes a prominent contribution from resonance scattering by alkali atoms—especially sodium (Na)—in addition to continuum scattering by dust particles. The relative contributions of these two components are crucial for estimating the total ejecta mass. Due to the strong response of the Na D-line emission (589 nm) in the R (600–700 nm) and G (500–600 nm) bands and the lack of response in the B (400–500nm) band, the color of the ejecta reddens notably post-impact.

In principle, the kinematic behavior of neutral Na atoms may differ significantly from that of solid dust grains, as their ejection mechanisms, coupling to radiation pressure, and possible interactions with the surrounding plasma environment, are distinct. However, given the limited current understanding of Na atom dynamics in the post-impact ejecta cloud, we adopt the assumption that sodium atoms follow the same velocity-to-mass distribution as the dust particles. Under this assumption, our simulated ejecta color parameters show good agreement with the observed post-impact photometric evolution (see Figure3c), supporting the practical validity of this approximation in the context of our model.

Prior to impact, the observed apparent magnitude was 14.48 ± 0.11, corresponding to a total irradiance of E_0. The measured color indices were approximately B–G = 0.25 ± 0.05, G–R = 0.25 ± 0.05, and B–R = 0.5 ± 0.05, suggesting a baseline reflectance ratio of $E_{B0} : E_{G0} : E_{R0} \approx 1 : 1.26 : 1.585$. These values are assumed to represent the intrinsic scattering properties of Dimorphos's surface material and are also used for modeling dust scattering ($E_{B,\mathrm{dust}} : E_{G,\mathrm{dust}} : E_{R,\mathrm{dust}}$) and slow ejecta components ($E_{B2} : E_{G2} : E_{R2}$).

At 184 seconds post-impact, the system reached its peak brightness (apparent magnitude m_v= 12.18 ± 0.03, irradiance E_1), with color indices shifting to B–G = 0.9 ± 0.05, G–R = 0.3 ± 0.05, and B–R = 1.2 ± 0.05, implying a new irradiance ratio of $E_{B1} : E_{G1} : E_{R1} \approx 1 : 2.29 : 3.02$. Following the departure of the fast ejecta from the photometric aperture, the color indices returned to their pre-impact values, and the system brightness dropped to m_v=

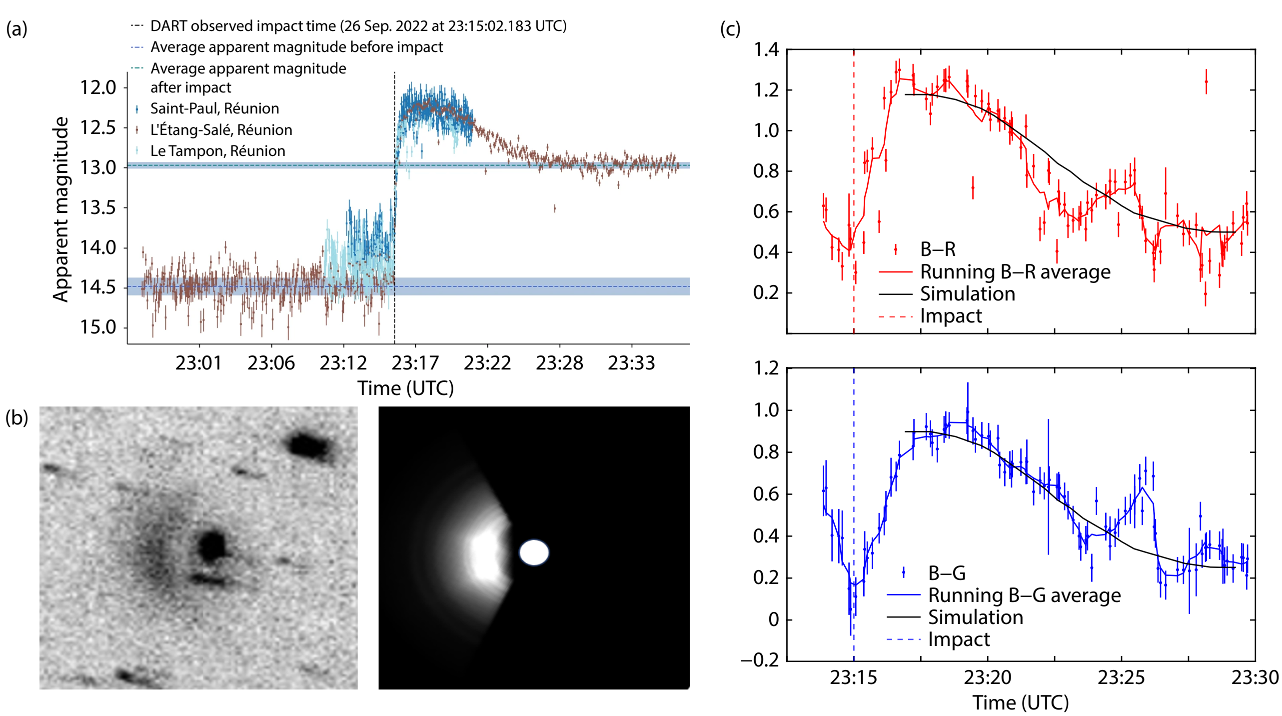

Figure 3. (a) Observed photometric brightness of the fast ejecta, reproduced from Graykowski et al. (2023). (b) Comparison between the observed morphology (left) (Ofek et al., 2023) and our simulation result (right) of the fast ejecta (T + 1848 s). (c) Comparison of the observed and simulated B–R and B–G color indices of the fast ejecta throughout the observation period, with error bars indicating observational uncertainties.

12.96 ± 0.04, corresponding to a total irradiance E_2.

This photometric analysis focuses on relative changes in brightness and color before and after the impact, and thus does not depend on the absolute spectral response of a specific telescope filter system. For this purpose, we adopt two key assumptions: (1) that Na resonance emission at the D-line (589 nm) contributes negligibly to the B band (400–500 nm), and (2) that the total visible-band irradiance at any given time is the sum of the irradiance in the B, G, and R bands (e.g. $E_0 = E_{B0} + E_{G0} + E_{R0}$). These assumptions enable us to estimate the relative contributions of atomic and dust scattering based on color and magnitude evolution alone:

$$\begin{cases} E_0 + (E_{B,\mathrm{dust}} + E_{G,\mathrm{dust}} + E_{R,\mathrm{dust}}) + E_{Na} = E_1 - E_2, \\ E_{B0} + E_{B,\mathrm{dust}} = E_{B1} - E_{B2}. \end{cases} \tag{10}$$

Solving this system yields an estimated response ratio of approximately 1.33 : 1 for the D-line emission in the R and G bands, consistent with expectations based on the camera's relative spectral sensitivity to the 589 nm sodium line (Poggiali et al., 2022). These results indicate that resonance scattering by alkali atoms—primarily sodium—accounts for ~76.2 ± 4.3% of the fast ejecta brightness, while the remaining ~23.8 ± 4.3% arises from sunlight scattered by dust grains. To further validate this interpretation, we calculated the B–R and B–G color indices of the fast ejecta using the derived brightness ratio, and compared them with the observed color evolution (as shown in Figure 3c). The modeled color indices match the observational data well throughout the entire monitoring period of the fast ejecta. This agreement supports our assumption that the color variation of the fast ejecta is primarily driven by resonance scattering from sodium atoms, and further confirms the robustness of the estimated brightness ratio.

From the observed picture, we construct a geometric model of the fast ejecta plume, approximated as a spherical cap with an opening angle of ~130°. A comparison between synthetic images generated using this velocity model and observational data is shown in Figure 3b. In addition, Figure 3c presents a comparison between the observed color indices (B–R, G–R) reported by Graykowski et al. (2023) and the simulated color evolution derived from our model. We note that the observed B–R and B–G time series contain short-timescale excursions that our ejecta model does not reproduce (such as the raised pattern at the time of 23:25). Since these data were collected by external observers, we do not have access to the raw frames or observing logs to pinpoint the exact cause of each anomaly. Potential contributors include unmasked background stars or planets drifting through the photometric aperture, transient changes in sky transparency (e.g., thin cirrus or aerosol layers). Although these factors introduce occasional spikes in the color curves, they do not affect the overall trend—namely, the rapid post-impact reddening followed by a gradual return toward pre-impact values—which remains in excellent agreement with our simulation. Therefore, we focus our analysis on this dominant photometric evolution, through which we infer the role of ejecta composition in driving the color changes. The morphological agreement and the satisfactory match of color indices, together, provide supporting evidence for the reliability of our ejecta modeling and momentum estimation.

Due to the limited data, the particle size distribution of the fast ejecta remains uncertain and can be constrained only via kinetic energy limits. High-speed particles cannot have excessively large sizes, as this would result in unreasonably high kinetic energy. For instance, assuming an average particle radius of 5 μm would imply a kinetic energy exceeding 90% of the impactor's total energy. Conversely, particles of radius smaller than ~0.5 μm are also invalid due to their low ratio in kinetic energy. Based on both photometric and energetic constraints, we adopt a fiducial particle radius of 1 μm and a plausible range of 0.5–1.5 μm to account for the uncertainty. Within this interval, the modeled energy fraction carried by fast ejecta varies from approximately 7.8% to 23.4%. Under the 1 μm assumption—matching the minimum size for slow ejecta—the total mass of the fast ejecta is estimated to be ~660 ± 330 kg, contributing ~15.6% of the total impactor energy. Assuming a uniform probability distribution across the considered size range, this translates to an estimated uncertainty of ± 7.8% in the energy contribution. This proportion of kinetic energy is broadly consistent with prior modeling studies (>10%) based on post-impact photometric evolution (Gault et al., 1963; O'Keefe and Ahrens, 1977). Given that other input parameters (e.g., total ejecta brightness, velocity distribution, and spectral color indices) are better constrained by observational data, we attribute to this range the dominant source of uncertainty in our fast ejecta model.

We next compare this estimate with previous observational and modeling efforts. Graykowski et al. (2023) estimated a fast ejecta dust mass of ~700 ± 120 kg for 0.1 μm particles and ~7000 ± 1200 kg for 1 μm particles, assuming that all brightness originated from dust scattering. Weaver et al. (2024), based on photometric data from the Lucy spacecraft, calculated a total dust mass of ~380 kg. This value is slightly lower than ours due to the omission of dust scattering in their model.

Under this model, the fast ejecta is estimated to account for β_{fast} = 0.241 ± 0.121 of the impactor momentum; this estimate's uncertainty arises primarily from the poorly constrained mean particle size in the fast ejecta simulation. Key parameters used in the modeling are summarized in Table 3.

4.2 The Slow Ejecta

The size range of the slow ejecta spans from micrometer to meter. Based on the observed tail length and the size-sorting effect of solar radiation pressure, Li JY (2023) and Moreno (2023) inferred that particles as small as 2 μm can account for the tail's extent and structure. Their models suggest a broken power-law size distribu-

Table 3. Physical properties of the fast ejecta.

Parameter	Value
Particle radius (μm)	1 ± 0.5
Ejection velocity (km/s)	1–4
Ejection angle (°)	0–65
Total mass (kg)	660 ± 330
Kinetic energy contribution (%)	15.6 ± 7.8
Momentum enhancement factor β_{fast}	0.241 ± 0.121

tion, with an index of $q_1 = -2.7 \pm 0.2$ for particles between d_1 = 2 µm and d_2 = 6 mm, and $q_2 = -3.7 \pm 0.2$ for larger than d_2 =6 mm. To maintain size continuity in our subsequent discussion of meter-scale boulders, we adopt a conservative extrapolation of the q_2 up to d_3 =1 m. This broken power-law was originally derived from photometric modeling of the anti-solar dust tail, which is composed primarily of slower particles subject to strong solar radiation pressure. In contrast, our dynamical model adopts the point-source scaling framework of Housen and Holsapple (2011), in which the initial ejection speed of particles is treated as independent of their size. Under this assumption, it is reasonable to extend the tail-inferred size distribution to represent the entire slow ejecta population.

$$N(d) = \begin{cases} N_0 d^{q_1}, & d_1 \le d \le d_2, \\ CN_0 d^{q_2}, & d_2 \le d \le d_3, \end{cases} \tag{11}$$

where C is the ratio of the particle number in the size interval. The total optical brightness of the slow ejecta is attributed entirely to dust scattering. Submeter particles dominate the optical signal of the slow ejecta, accounting for nearly all of the observed scattering cross-section. Although meter-sized boulders may carry significant mass, they contribute less than 0.3% to the total brightness and are thus excluded from the photometric model.

To estimate the total ejecta mass, we apply the radiative transfer formulation Equation (9) introduced in Section 3, which relates the increase in brightness to an increase in total scattering area. The post-impact magnitude increase from m_v = 14.48 ± 0.11 to m_v = 12.96 ± 0.04 corresponds to an increase in scattering cross-section of approximately S_{slow} =0.37 ± 0.2 km^2. Given the established size distribution and integration limits, the corresponding total particle volume is calculated using the following expression for a broken power-law:

$$N_0 = \frac{4S_{\text{slow}}(q_1+3)(q_2+3)}{\pi\left[(q_2+3)\left(d_2^{q_1+3}-d_1^{q_1+3}\right)+C(q_1+3)\left(d_3^{q_2+3}-d_2^{q_2+3}\right)\right]}, \tag{12}$$

$$V_{\text{slow}} = \frac{\pi N_0}{6}\left[\frac{d_2^{q_1+4}-d_1^{q_1+4}}{q_1+4}+C\frac{d_3^{q_2+4}-d_2^{q_2+4}}{q_2+4}\right]. \tag{13}$$

The computed total volume is 4316.2 ± 233.3 m^3. Spectral analysis indicates that Dimorphos is compositionally similar to S-type L/LL ordinary chondrites (Dunn et al., 2013), supporting a material density of ~3400 kg/m^3 for mass estimation. Accordingly, the total mass of sub-meter slow ejecta is estimated to be (1.47 ± 0.08) × 10^7 kg.

Unlike the fast ejecta, the slow ejecta, due to their lower velocities and prolonged motion time (up to ~25 days), are significantly influenced by the gravitational field of the binary system and solar radiation pressure, resulting in complex, non-linear trajectories. Given these dynamical complexities and their extended spatial distribution, we define their initial velocity distribution using the point-source scaling law introduced in Supplementary Materials, which relates ejecta velocity to launch position based on the target and impactor properties. We assume that the DART impact formed a crater under strength-dominated conditions, with a strength–gravity transition at Y_0 = 4 Pa (Raducan et al., 2024). The impactor is modeled as a spherical projectile with radius 0.517 m, density 1000 kg/m^3, and mass 579.4 kg, impacting Dimorphos at 6145 m/s. The material parameters used in the cratering model are listed in Table 4. While these parameters are not currently measured, the adopted values represent our best-fit estimates derived from available observational constraints and theoretical scaling relations, which will be discussed further in Section 5.

Following the axisymmetric assumption discussed earlier, the slow ejecta is modeled as a conical plume with an opening angle of 125° ± 10°, originating from the impact point and emitted radially outward at distance x. The particle sampling uses the hybrid method introduced in Section 3.1, ensuring no fewer than 10^7 tracer particles are sampled across the 2 µm to 1 m size range. These are used for dynamical evolution and imaging simulation.

Figure 4 presents the simulated images at four time. We find that the scaling-law-based initial conditions for the slow ejecta successfully reproduce the major morphological features observed, including the two northeast-pointing edge rays of the ejecta cone and the elongated anti-solar dust tail. In addition, the observed images show a pair of symmetric radial spikes, which are not modeled here. These features are diffraction artifacts introduced by the telescope's support structure and do not represent actual ejecta brightness (Li JY et al., 2023). Notably, a secondary tail structure approximately 4° north of the main tail emerges around T + 5 days (where T is the epoch of the DART impact on Dimorphos), forming a distinct fan-shaped morphology centered on the Didymos system. This structure is consistent with observations from space-based telescopes, as shown in Figure 5.

Our imaging model presented in Figure 5 does not include generation of secondary ejecta from re-impacts on the binary components, though such secondary ejecta do contribute non-negligibly to the total brightness at later times and are included in the photometric simulations presented in Section 5. Here, we focus solely on reproducing the morphological features of the ejecta cloud. The ability of the model to reproduce the secondary tail without invoking additional impact-generated material suggests that such processes are not strictly required to explain the observed structure. Instead, the morphology could plausibly result just from the combined influence of binary gravity and solar radiation pressure acting on the slow ejecta. Consequently, the

Table 4. Parameters adopted in crater scaling law modeling.

Parameter	Value	Reference
Dimorphos bulk density (kg/m^3)		
Dimorphos matrix cohesion (Pa)	2400	See Section 5
Crater scaling parameters μ		
Crater scaling parameters C_1		
v		
n_1		
n_2		
k	0.4	Cheng AF et al., (2024)
p		
H_2		

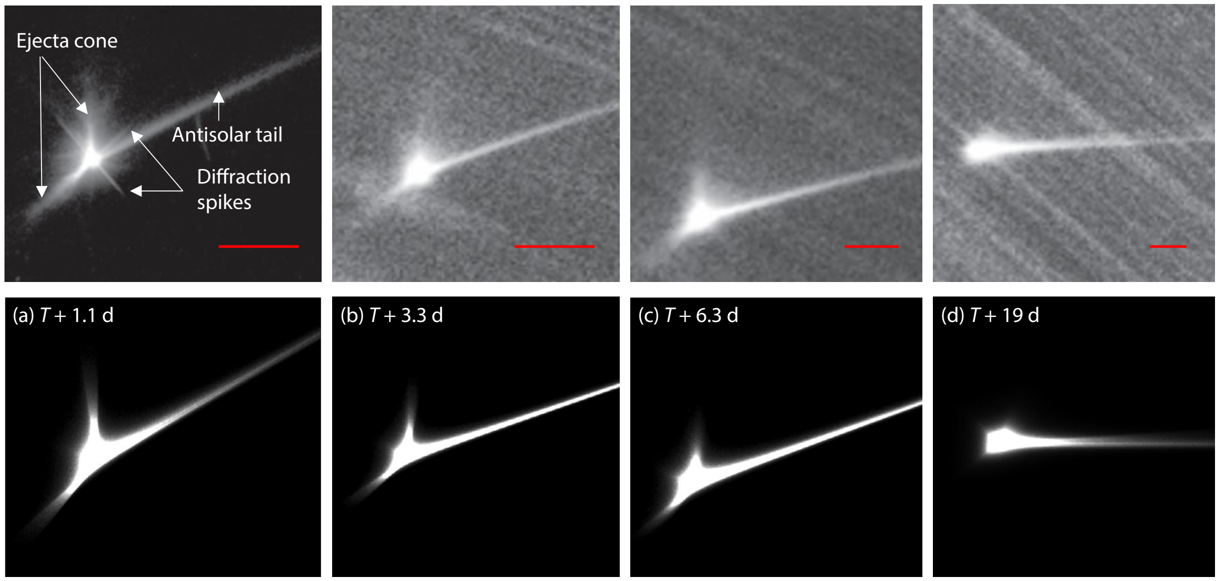

Figure 4. Comparison of observed and simulated morphologies of the slow ejecta at four different epochs. Observational data are from HST and Spaceobs (Moreno et al., 2023). In the first observation image, the red line represents a scale of 200 km, while in the second, third, and fourth observation images, the red line represents 2000 km. The scales of the observations and simulations have been adjusted to be consistent across all time points.

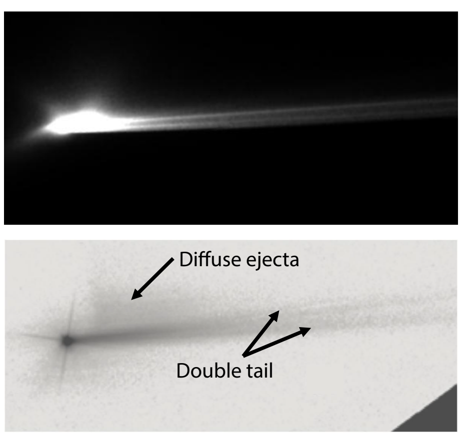

Figure 5. Comparison between simulated (*T*+11.82 d) and observed (HST, Moreno et al., 2023) secondary tail.

secondary tail may encode information about the particle size and velocity distributions, although the lack of reliable brightness measurements limits our ability to quantitatively constrain these properties.

Given that Dimorphos has an escape velocity of ~0.09 m/s, a very small fraction of the particles in our study (less than 0.1%) failed to escape Dimorphos's gravity, indicating a negligible gravitational influence. Since we are concerned primarily with momentum transfer to Dimorphos rather than with the Didymos system as a whole, the initial momentum of the escaping slow ejecta provides a valid approximation of the momentum change imparted to Dimorphos. Under this condition, the momentum enhancement factor for the slow ejecta is β_{slow} = 2.92 ± 0.05, and the total kinetic energy of this component corresponds to 1.31 ± 0.02% of the impactor's energy.

It is worth noting that the scaling law used here lacks an explicit relation between particle size and ejection velocity. Due to technical limitations, laboratory experiments generally involve ejecta with sizes of mm or larger (Okawa et al., 2022), and thus cannot resolve how velocity depends on particle size. However, models by Li JY et al. (2023) and Moreno et al. (2023) suggest that an inverse power-law velocity–size relation is necessary to reproduce details such as the curvature of the ejecta cone's edge. Consequently, some fine-scale features in our simulations do not perfectly match the observations. Future studies aimed at fitting such details may offer valuable constraints on the velocity–size function at planetary scales.

4.3 The Boulder Swarm

Meter-scale boulders within the DART ejecta cloud have been independently identified in both LICIACube and HST observations. Farnham et al. (2023) reported numerous bright features in LUKE images, interpreted as submeter to ~5-meter boulders, with projected velocities on the order of tens to hundreds of meters per second. However, this interpretation remains tentative due to the lack of a peer-reviewed publication as of April 2025, and the markedly different velocity regime from HST observations raises uncertainty about the true nature of these features. Therefore, for quantitative modeling, we rely exclusively on the HST dataset by Jewitt et al. (2023).

Jewitt identified 37 individual boulders in HST images, with diameters up to 7 m and projected velocities ranging from 0.26 to 0.71 m/s (average: 0.38 m/s). These velocity estimates were derived by assuming straight-line, constant-speed motion of each boulder in the sky-plane, dividing the observed projected displacement by the time since impact. These projected velocities represent the motion after escaping the binary system. The initial launch speeds were then estimated using energy conservation.

Due to limitations in image resolution and background noise, only boulders larger than ~4 m could be reliably detected in the HST dataset. Assuming a material density of 3400 kg/m^3, the resolved 4–7 m boulders correspond to a total volume of ~1206 m^3 and an estimated mass of ~4 × 10^6 kg. To account for unresolved boulders down to 1 m, we adopt a differential size distribution power law with index −2.8 ± 0.2, which is derived from pre-impact surface images of Dimorphos. This yields a total boulder mass of (7.58 ± 0.30) × 10^6 kg for the 1–7 m size range.

The fate of these boulders was studied by Moreno et al. (2024), who analyzed their dynamical evolution up to T + 83 days (2022-12-29). Their results suggest that ~85% of the meter-sized boulders escaped the binary system, while ~6% re-impacted Dimorphos. Assuming that the boulders identified in HST images represent the escaped population, we scale the observed mass accordingly to estimate a total ejected boulder mass of (8.91 ± 0.35) × 10^6 kg. This accounts for 37.8 ± 1.6% of the total ejecta mass (2.37 ± 0.09) × 10^7 kg. The result is consistent with prior estimates by Graykowski et al. (2023) and Roth et al. (2023), and further supports the conclusion that the bulk of ejecta mass was carried by slow, submeter particles.

To quantify the momentum contribution of meter-sized boulders, we assume that they were launched together with the slow ejecta in a conical outflow. The ejecta cone is modeled with a half-opening angle of 62.5° ± 5°, aligned with the nominal impact axis. Boulders are assigned initial velocities uniformly distributed between 0.26 and 0.71 m/s and placed randomly within the cone. The dynamical simulation spans 100 days post-impact, including the gravitational field of the Didymos–Dimorphos binary and solar radiation pressure, although the latter has negligible effect on meter-scale bodies.

No fewer than 10^6 tracer particles are sampled within the 1–7 m diameter range to represent the full mass distribution. To constrain individual boulder speeds, we divided the tracer particles into six initial velocity bins and plotted their projected spatial distributions separately. The observed boulder positions were then compared to these distributions to infer their likely speed ranges (see Figure 6a, b).

Figure 6c compares the sky-plane positions of simulated boulders with HST detections. The distribution is markedly anisotropic, with both modeled and observed boulders clustering in the western and southern sectors. Two azimuthal peaks are evident at ~90° and ~270°, consistent with preferred ejection directions within a conical geometry. This directional agreement between simulations and observations supports the hypothesis that the meter-scale boulders were launched within the slow ejecta cone. Although the overall distribution pattern and the locations of azimuthal peaks are reasonably well reproduced, the modeled angular profile does not perfectly match the observed one. Given the limited number of resolved boulders (~37), such discrepancies are considered acceptable within the expected statistical uncertainty.

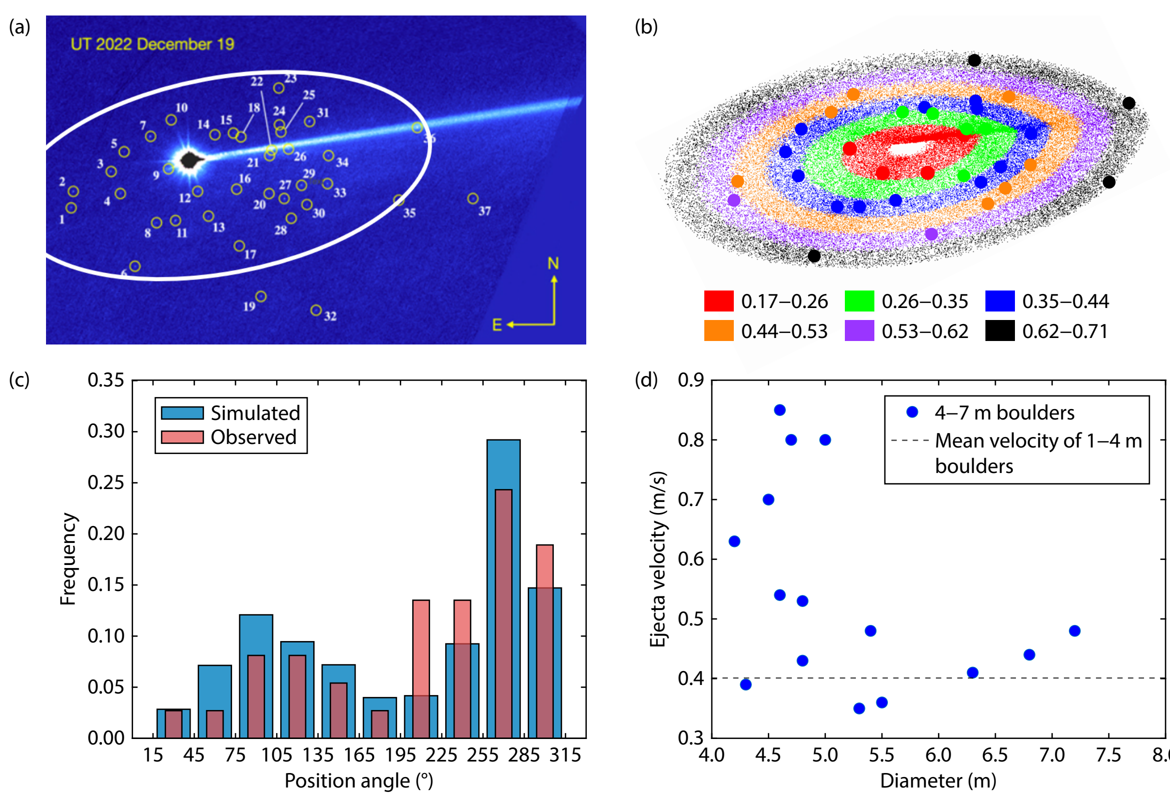

Figure 6. (a) HST boulder distribution in 2022-12-18 (Jewitt et al., 2023). The white contour-enclosed region in the figure represents the coverage area of the tracer particles, with only three boulders not covered; (b) simulated spatial distribution. Tracer particles with different ejection velocity (m/s) ranges are marked in different colors; the positions of meter-sized boulders observed by HST are indicated by colored dots of corresponding colors; (c) boulder and tracer azimuthal density; (d) velocity–size distribution of 4–7 m boulders and average velocity of 1–4 m boulders.

For boulders in the 4–7 m size range, individual particle diameters can be directly resolved from HST imagery. By assigning to each resolved velocity a corresponding diameter, we constructed a two-dimensional distribution in size–velocity space and directly obtained the total momentum of this population. For boulders in the 1–4 m size range, individual diameters cannot be directly resolved. Instead, we adopted an average velocity of approximately 0.40 ± 0.03m/s based on their spatial distribution (see Figure 6d). Combined with the previously estimated total mass for this population, we derived their total momentum contribution. The total momentum of all meter-scale boulders was computed as the sum of the two contributions above, representing the combined effect of both resolved and unresolved fragments in this size regime.

It is worth noting that, in Section 5, the total mass of the secondary ejecta is estimated based on the post-impact photometric decay curve. This empirically-derived estimate thus imposes no constraints on the physical origin of the secondary ejecta—whether it arises from fine dust or from larger fragments such as the meter-scale boulders discussed in this section. Jewitt et al. (2023) reported that all boulders observed 83 days after impact exhibited speeds exceeding the system's escape velocity (~0.24 m/s). If any boulders were ejected with velocities below the system's escape speed (~0.24 m/s), they would likely undergo short-term orbital evolution and eventually re-impact the surface of Didymos or Dimorphos. Such secondary impacts could potentially equal a fraction of the secondary ejecta observed. However, given the small number of identified boulders (37 in total), it remains uncertain whether any of them have actually returned and collided with the binary system. A definitive identification of such processes may be feasible in the future, based on shape and crater mapping by Hera.

Under these assumptions, meter-scale boulders carry approximately <0.01% of the DART impactor's kinetic energy and contribute $\beta_{\text{boulder}} = 0.439 \pm 0.023$ of impactor momentum. This result reflects their large mass and low velocity, consistent with expectations for this ejecta population. By modeling these boulders independently, we address the challenge posed by their negligible contribution to observed brightness, which makes it difficult to constrain their total mass, momentum, and energy through photometry alone. The analysis demonstrates that, despite their limited radiative signature, meter-scale boulders represent a significant fraction of the total momentum budget—highlighting the necessity of incorporating them into momentum decomposition frameworks.

5. Physical Characterization of Dimorphos Based on Ejecta Modeling

As discussed in Section 4.2, the submeter slow ejecta were modeled using the point-source cratering scaling law developed by Housen and Holsapple (2011), which establishes a deterministic relationship between ejecta velocity, total ejected mass, and the physical properties of the target body. In this section, we constrain the intrinsic properties of Dimorphos, including its bulk density (ρ), material strength (Y), and dimensionless cratering coefficients (e.g., μ, ν, C_1, n_1), using multi-source photometric observations. These results are applied within the hierarchical momentum decomposition framework developed in this study and are compared with previous simulation-based estimates (Cheng AF et al., 2020, 2022, 2024; Raducan et al., 2024) and SPH-derived constraints to assess the consistency and robustness of our approach.

We begin by identifying the key free parameters in our inversion. The bulk density ρ and strength Y of Dimorphos are treated as the primary variables. Among the cratering parameters, μ and C_1 significantly affect ejecta velocity (see Equation (A3)), and are thus retained as adjustable inputs. The remaining parameters are fixed as follows: ν, n_1, n_2, and k are assigned standard values reported by Housen and Holsapple (2011), as their variations across different materials are negligible. Although p, H_1, and H_2 exhibit some material dependence, their influence on the ejecta velocity is limited, and they are thus held constant in this study, based on Bern SPH simulations from Raducan et al. (2024). The total mass of the slow ejecta, constrained to $1.47 \pm 0.08 \times 10^7$ kg from photometric analysis, and the maximum ejecta velocity of ~500 m/s inferred from LUKE imaging data (Dotto et al., 2024), together, impose strong constraints on the velocity–mass relations defined in Equations (A3) and (A4). These observational bounds effectively reduce the dimensionality of the parameter space to two dominant variables—ρ and Y.

To incorporate photometric constraints, we adopt the post-impact brightness decay curve published by Kareta et al. (2023). The fitting metric is defined as the sum of squared residuals between the simulated and observed flux values. We then perform a grid search over the two-dimensional (ρ, Y) parameter space, visualizing the residual values as a 2D heatmap. This residual map allows us to identify the parameter combination that best reproduces the observed light curve. The best-fit brightness decay curve and the corresponding two-dimensional residual map are shown in Figure 7a and Figure 7b, respectively.

To account for the temporary flattening in brightness decline reported by Kareta et al. (2023), we introduce a secondary ejecta component, adopting a conservative mass estimate of 8×10^5 kg based on previous studies (Ferrari et al., 2022; Moreno et al., 2023). This secondary component is modeled as isotropic, low-speed (<0.24 m/s) emission from the surface of Didymos, spanning the interval from Day 5 to Day 10 post-impact. As these particles are gravitationally bound to the binary system, they do not contribute to momentum transfer but do affect the in-aperture brightness evolution.

The best-fit parameters obtained from this photometric inversion are: bulk density $\rho = 2400 \pm 100$ kg/m^3, strength $Y = 120 \pm 20$ Pa, and cratering parameters $\mu = 0.470 \pm 0.005$ and $C_1 = 0.42 \pm 0.03$. Under this physical parameter configuration, combined with the momentum analysis in Section 4, the total momentum of all ejecta results in a coefficient β of 3.60 ± 0.13. These values are presented alongside prior estimates in Table 5 for comparison, including simulated results from Cheng AF et al. (2020, 2022, 2023, 2024), Roth et al. (2023), Graykowski et al. (2023), Daly et al. (2023), and Raducan et al. (2024). The inferred parameters fall within expected ranges and provide a self-consistent fit to the observational data, supporting the viability of our inversion

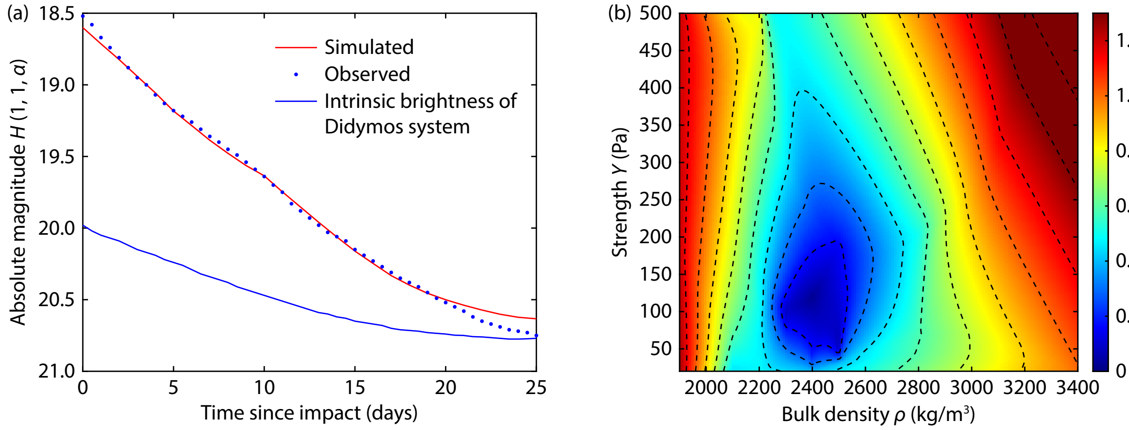

Figure 7. (a) Comparison between observed (from Kareta et al., 2023) and modeled brightness decay curve. The plotted magnitudes are corrected for heliocentric and geocentric distances but still include phase angle effects. For comparison, the intrinsic brightness evolution of the Didymos system (H = 18.16, G_1 = 0.84, G_2 = 0.05; Hasselmann et al., 2024) is shown as a solid blue line. In the late stage of ejecta dissipation (20–25 days post-impact), the simulated brightness slightly exceeds the observations, which may be attributed to noise and integration time effects as discussed in Section 3.3. (b) 2D residual map over (ρ, Y) parameter space.

Table 5. Comparison of inferred model parameters with previous studies.

Physical parameter	Simulation result	Previous studies
Ejecta mass (10^7 kg)	2.37 ± 0.09	0.9–5.5 (Roth et al., 2023)
Dimorphos bulk density (kg/m³)	2400 ± 100	1500–3400 (Cheng AF et al., 2023)
Strength Y (Pa)	120 ± 20	5–500 (Raducan et al., 2024)
Momentum transfer coefficient β	3.60 ± 0.13	3.61 (Cheng AF et al., 2023)
Crater scaling parameters μ	0.470 ± 0.005	0.45 ± 0.02 (Cheng AF et al., 2024)
Crater scaling parameters C_1	0.42 ± 0.03	0.47 (Cheng AF et al., 2024)
Ejecta kinetic energy fraction (%)	16.9 ± 7.8	>10 (O'Keefe and Ahrens, 1977)

framework.

6. Conclusion and Discussion

This study presents a comprehensive methodology for analyzing momentum transfer in asteroid kinetic impact events, using the DART mission as a case. We developed a photometry-driven simulation framework that integrates ejecta sampling, dynamical propagation, and synthetic imaging; this approach enables direct comparison of its output with multi-platform observational datasets.

By decomposing the ejecta into three physically distinct components—high-velocity atomic plumes, low-velocity conical ejecta, and meter-scale boulders—we independently constrained their velocity distributions, mass, and momentum contributions. The fast ejecta fraction was modeled through photometric decay curves combined with resonance scattering analysis, identifying sodium D-line emission as the dominant contributor to the observed brightness. Under the assumed average radius of 1 ± 0.5 μm, the fast ejecta was found to carry approximately 15.6% ± 7.8% of the impactor's energy and exhibited a momentum enhancement factor β_{fast} = 0.241 ± 0.121. The slow ejecta, spanning from 2 μm to 1 m, dominated the total ejecta mass (1.47 ± 0.08) × 10^7 kg and produced a best-fit momentum contribution β_{slow} = 2.92 ± 0.05. Meanwhile, meter-sized boulders, despite contributing only marginally to the total brightness, accounted for a significant mass (8.91 ± 0.35) × 10^6 kg and momentum contribution $\beta_{boulder}$ = 0.470 ± 0.005. The combined total momentum enhancement factor inferred was β = 3.60 ± 0.13, consistent with independent estimates from dynamical measurements. The substantial differences observed between fast ejecta, slow ejecta, and boulders in terms of brightness, morphology, mass, velocity, and momentum underscore the critical importance of hierarchical ejecta decomposition in reconstructing the true momentum transfer efficiency of kinetic impact events.

By reconstructing the initial size–velocity distributions and applying point-source cratering scaling law, we achieved satisfactory fits to both the observed photometric decay curves and morphological features over the first month post-impact, and thus have constrained key physical parameters of Dimorphos. The best-fit values obtained were a bulk density of ρ = 2400 ± 100 kg/m³, an effective material strength of Y = 120 ± 20 Pa, and cratering parameters μ = 0.470 ± 0.005 and C_1 = 0.42 ± 0.03. These estimates align well with prior simulation-based studies (Cheng AF et al., 2020, 2022, 2023, 2024; Roth et al., 2023, Graykowski et al., 2023, Daly et al., 2023, Raducan et al., 2024), validating the feasibility of photometric inversion as a tool for probing the internal structure and mechanical properties of small bodies such as Dimorphos.

In the future, we plan to extend the modeling framework established in this study to incorporate more realistic ejection dynamics, including angular anisotropies, local surface topography, and particle size–velocity correlations derived from laboratory experiments or in-situ observations. We also aim to refine the treatment of secondary ejecta from re-impacts by incorporating more detailed gravitational and surface interaction models. In addition, we plan to implement models that are more physically representative of light scattering and solar radiation pressure, accounting for the dependence of scattering behavior on particle size and composition. These improvements will enhance the physical fidelity of ejecta simulations and reduce uncertainties in momentum transfer estimates. Since photometric modeling of ejecta serves as a powerful tool for validating deflection outcomes and characterizing asteroid properties, it should be incorporated in the planning of future planetary defense missions as a cost-effective supplement to direct measurements. This approach will improve the reliability of impact-based strategies and maximize scientific return during mission planning and post-impact assessment.

Based on this framework, we recommend the use of rapid-response precursor missions—including low-energy test impacts—for high-risk targets identified through early-warning systems, enabling early assessment of surface properties and more reliable deflection mission planning.

Supplementary Materials

Point-Source Scaling of DART Impact Ejecta

The outcome of a hypervelocity impact, particularly the distribution of ejecta mass and velocity, depends on various parameters, including surface and subsurface properties of the target. In this study, the ejecta distribution is modeled using the scaling laws described by Housen and Holsapple (2011), which are derived from laboratory experiments across a wide range of impact conditions.

For a spherical projectile of mass m and radius a impacting a planar target vertically at velocity U, the resulting crater radius R depends on the target density ρ and a set of dimensionless cratering parameters. Under gravity-dominated or strength-dominated regimes, R is expressed as:

$$R\left(\frac{\rho}{m}\right)^{\frac{1}{3}} = H_1\left(\frac{\rho}{\delta}\right)^{\frac{2+\mu-6\nu}{3(2+\mu)}}\left(\frac{ga}{U^2}\right)^{-\frac{\mu}{2+\mu}}, \tag{A1}$$

$$R\left(\frac{\rho}{m}\right)^{\frac{1}{3}} = H_2\left(\frac{\rho}{\delta}\right)^{\frac{1-3\nu}{3}}\left(\frac{Y}{\rho U^2}\right)^{-\frac{\mu}{2}}. \tag{A2}$$

Here, Y is the target strength, δ is the projectile density, and μ, ν, H_1, and H_2 are dimensionless scaling parameters. The porosity-dependent parameter μ (typically 1/3 to 2/3) spans the momentum-to-energy scaling limits. The parameter ν depends on the density ratio and is usually taken as 0.4. The transition between gravity- and strength-dominated cratering occurs when the two estimates of R from Equation (A1) and Equation (A2) are equal. Notably, as a rubble-pile body, Dimorphos's strength in this context represents an effective cohesion arising from regolith friction and boulder interlocking, rather than the monolithic tensile strength of solid rock. The ejection speed v at a radial distance x from the impact point, normalized by the impact velocity U, is given by:

$$\frac{v}{U} = C_1\left[\frac{x}{a}\left(\frac{\rho}{\delta}\right)^{\nu}\right]^{-\frac{1}{\mu}}\left(1-\frac{x}{n_2 R}\right)^{p},\ n_1 a < x < n_2 R, \tag{A3}$$

where C_1 and p are dimensionless scaling parameters. The cumulative mass distribution $M(<x)$ defines the total mass of ejecta launched from within a radial distance x of the impact point, corresponding to all ejecta with speeds greater than that at x. It is defined by:

$$M(x) = m\frac{3k}{4\pi}\frac{\rho}{\delta}\left[\left(\frac{x}{a}\right)^3 - {n_1}^3\right],\ n_1 a < x < n_2 R. \tag{A4}$$

The distribution includes both lower and upper cutoff radii corresponding to $x = n_1 a$ and $x = n_2 R$, respectively, where n_1 and n_2 are model constants. The values of the scaling parameters ($\mu, \nu, H_1, H_2, C_2, k$, and p) are empirically determined by fitting laboratory impact experiments (Housen and Holsapple, 2011). While this study adopts the point-source cratering formulation for modeling, we emphasize that our framework does not rely on any particular scaling law. Instead, it accommodates any empirical or analytical formulation describing the size–velocity distribution of impact ejecta.

Acknowledgments

This work was supported by the National Natural Science Foundation of China (Grant No. 12272018) and the National Key Basic Research Project (2022JCJQZD20600).

References

Bagnulo, S., Gray, Z., Granvik, M., Cellino, A., Kolokolova, L., Muinonen, K., Muñoz, O., Opitom, C., Penttilä, A., and Snodgrass, C. (2023). Optical spectropolarimetry of binary asteroid Didymos–Dimorphos before and after the DART impact. *Astrophys. J. Lett.*, *945*(2), L38. https://doi.org/10.3847/2041-8213/acb261

Burattini, C., Colombo, C., and Trisolini, M. (2024). Aerogel-based collection of ejecta material from asteroids from libration point orbits: Dynamics and capture design. *Astrodynamics*, *8*(4), 529–551. https://doi.org/10.1007/s42064-023-0197-x

Burns, J. A., Lamy, P. L., and Soter, S. (1979). Radiation forces on small particles in the solar system. *Icarus*, *40*(1), 1–48. https://doi.org/10.1016/0019-1035(79)90050-2

Capek, D., and Vokrouhlický, D. (2004). Accurate model for the Yarkovsky effect. *Proc. Int. Astron. Union*, *2004*(IAUC197), 171–178. https://doi.org/10.1017/S1743921304008622

Chabot, N. L., Rivkin, A. S., Cheng, A. F., Barnouin, O. S., Fahnestock, E. G., Richardson, D. C., Stickle, A. M., Thomas, C. A., Ernst, C. M., … Zhang, Y. (2024). Achievement of the planetary defense investigations of the double asteroid redirection test (DART) mission. *Planet. Sci. J.*, *5*(2), 49. https://doi.org/10.3847/PSJ/ad16e6

Cheng, A. F., Stickle, A. M., Fahnestock, E. G., Dotto, E., Della Corte, V., Chabot, N. L., and Rivkin, A. S. (2020). DART mission determination of momentum transfer: Model of ejecta plume observations. *Icarus*, *352*, 113989. https://doi.org/10.1016/j.icarus.2020.113989

Cheng, A. F., Raducan, S. D., Fahnestock, E. G., Dotto, E., Della Corte, V., and Stickle, A. M. (2022). Model of double asteroid redirection test impact ejecta plume observations. *Planet. Sci. J.*, *3*(6), 131. https://doi.org/10.3847/PSJ/ac66e9

Cheng, A. F., Agrusa, H. F., Barbee, B. W., Meyer, A. J., Farnham, T. L., Raducan, S. D., Richardson, D. C., Dotto, E., Zinzi, A., … Zanotti, G. (2023). Momentum transfer from the DART mission kinetic impact on asteroid Dimorphos. *Nature*, *616*(7957), 457–460. https://doi.org/10.1038/s41586-023-05878-z

Cheng, A. F., Raducan, S. D., Jutzi, M., Farnham, T. L., Dotto, E., Della Corte, V., Mazzotta Epifani, E., Rossi, A., Gai, I., … Zannoni, M. (2024). DART impact ejecta plume evolution: Implications for Dimorphos. *Planet. Sci. J.*, *5*(5), 118. https://doi.org/10.3847/PSJ/ad4153

Cheng, B., Asphaug, E., Yu, Y., and Baoyin, H. (2023). Measuring the mechanical properties of small body regolith layers using a granular penetrometer. *Astrodynamics*, *7*(1), 15–29. https://doi.org/10.1007/s42064-021-0127-8

Daly, R. T., Ernst, C. M., Barnouin, O. S., Chabot, N. L., Rivkin, A. S., Cheng, A. F., Adams, E. Y., Agrusa, H. F., Abel, E. D., … Zhang, Y. (2023). Successful kinetic impact into an asteroid for planetary defence. *Nature*, *616*(7957), 443–447. https://doi.org/10.1038/s41586-023-05810-5

Daly, R. T., Ernst, C. M., Barnouin, O. S., Gaskell, R. W., Nair, H., Agrusa, H., Chabot, N. L., Cheng, A. F., Dotto, E., … Liciac. (2024). An Updated Shape Model of Dimorphos from DART Data. *Planet. Sci. J.*, *5*(1), 24. https://doi.org/10.3847/PSJ/ad0b07

Deshapriya, J. D. P., Hasselmann, P. H., Gai, I., Hirabayashi, M., Dotto, E., Rossi, A., Zinzi, A., Corte, V. D., Bertini, I., … Zanotti, G. (2023). Characterization of the DART impact ejecta plume on Dimorphos from LICIACube observations. *Planet. Sci. J.*, *4*(12), 231. https://doi.org/10.3847/PSJ/ad09ba

Dotto, E., Deshapriya, J. D. P., Gai, I., Hasselmann, P. H., Mazzotta Epifani, E., Poggiali, G., Rossi, A., Zanotti, G., Zinzi, A., … Zannoni, M. (2024). The Dimorphos ejecta plume properties revealed by LICIACube. *Nature*, *627*(8004), 505–509. https://doi.org/10.1038/s41586-023-06998-2

Dunn, T. L., Burbine, T. H., Bottke, W. F., and Clark, J. P. (2013). Mineralogies and source regions of near-Earth asteroids. *Icarus*, *222*(1), 273–282. https://doi.org/10.1016/j.icarus.2012.11.007

Fahnestock, E. G., Cheng, A. F., Ivanovski, S., Michel, P., Raducan, S. D., Rossi, A., Abell, P. A., Chesley, S., Dotto, E., … Zhang, Y. (2022). Pre-encounter predictions of DART impact ejecta behavior and observability. *Planet. Sci. J.*, *3*(9), 206. https://doi.org/10.3847/PSJ/ac7fa1

Farnham, T. L., Hirabayashi, M., Deshapriya, J. D. P., Barnouin, O. S., Bruck-Syal, M., Cheng, A., Della Corte, V., Dotto, E., Epifani, E. M., … Zinzi, A. (2023). Spatial distribution of the boulders in the dart impact ejecta: A 3-D analysis. Lunar and Planetary Science Conference Abstracts, 54, 2806 (#2426). https://ui.adsabs.harvard.edu/abs/2023LPICo2806.2426F/abstract

Fehlberg, E. (1969). Klassische Runge-Kutta-Formeln fünfter und siebenter Ordnung mit Schrittweiten-Kontrolle. *Computing*, *4*(2), 93–106. https://doi.org/10.1007/BF02234758

Ferrari, F., Raducan, S. D., Soldini, S., and Jutzi, M. (2022). Ejecta formation, early collisional processes, and dynamical evolution after the DART impact on Dimorphos. *Planet. Sci. J.*, *3*(7), 177. https://doi.org/10.3847/PSJ/ac7cf0

Gault, D. E., Shoemaker, E. M., and Moore, H. J. (1963). Spray Ejected from the Lunar Surface by Meteoroid Impact. NASA Tech. Note D-1767, Washington, D.C. https://books.google.com.sg/books?id=dHyZxkQ2XIsC

Graykowski, A., Lambert, R. A., Marchis, F., Cazeneuve, D., Dalba, P. A., Esposito, T. M., O'Conner Peluso, D., Sgro, L. A., Blaclard, G., … Transom, I. M. (2023). Light curves and colours of the ejecta from Dimorphos after the DART impact. *Nature*, *616*(7957), 461–464. https://doi.org/10.1038/s41586-023-05852-9

Hartzell, C. M. (2019). Dynamics of 2D electrostatic dust levitation at asteroids. *Icarus*, *333*, 234–242. https://doi.org/10.1016/j.icarus.2019.05.013

Hasselmann, P. H., Della Corte, V., Pravec, P., Ieva, S., Gai, I., Perna, D., Deshapriya, J. D. P., Mazzotta-Epifani, E., Dotto, E., … Zanotti, G. (2024). The unusual brightness phase curve of (65803) Didymos. *Planet. Sci. J.*, *5*(4), 91. https://doi.org/10.3847/PSJ/ad2add

Hoerth, T., Schäfer, F., Thoma, K., Kenkmann, T., Poelchau, M. H., Lexow, B., and Deutsch, A. 2013. Hypervelocity impacts on dry and wet sandstone: Observations of ejecta dynamics and crater growth. *Meteorit. Planet. Sci., 48*(1), 23–32. https://doi.org/10.1111/maps.12044

Housen, K. R., and Holsapple, K. A. (2011). Ejecta from impact craters. *Icarus*, *211*(1), 856–875. https://doi.org/10.1016/j.icarus.2010.09.017

Hyland, D. C., Altwaijry, H. A., Ge, S., Margulieux, R., Doyle, J., Sandberg, J., Young, B., Bai, X., Lopez, J., and Satak, N. (2010). A permanently-acting NEA damage mitigation technique via the Yarkovsky effect. *Cosmic Res.*, *48*(5), 430–436. https://doi.org/10.1134/S0010952510050096

Jewitt, D., Kim, Y., Li, J., and Mutchler, M. (2023). The Dimorphos Boulder Swarm. *Astrophys. J. Lett.*, *952*(1), L12. https://doi.org/10.3847/2041-8213/ace1ec

Kareta, T., Thomas, C., Li, J. Y., Knight, M. M., Moskovitz, N., Rożek, A., Bannister, M. T., Ieva, S., Snodgrass, C., … Skiff, B. (2023). Ejecta evolution following a planned impact into an asteroid: The first five weeks. *Astrophys. J. Lett.*, *959*(1), L12. https://doi.org/10.3847/2041-8213/ad0fdd

Kopp, G., and Lean, J. L. (2011). A new, lower value of total solar irradiance: Evidence and climate significance. *Geophys. Res. Lett.*, *38*(1), L01706. https://doi.org/10.1029/2010GL045777

Li, J. Y., Hirabayashi, M., Farnham, T. L., Sunshine, J. M., Knight, M. M., Tancredi, G., Moreno, F., Murphy, B., Opitom, C., … Trigo-Rodríguez, J. M. (2023). Ejecta from the DART-produced active asteroid Dimorphos. *Nature*, *616*(7957), 452–456. https://doi.org/10.1038/s41586-023-05811-4

Li, X. Y., Scheeres, D. J., Qiao, D., and Liu, Z. X. (2023). Geophysical and orbital environments of asteroid 469219 2016 HO3. *Astrodynamics, 7*(1), 31–50. https://doi.org/10.1007/s42064-022-0131-7

Lin, Z. Y., Vincent, J. B., and Ip, W. H. (2023). Physical properties of the Didymos system before and after the DART impact. *Astron. Astrophys.*, *676*, A116. https://doi.org/10.1051/0004-6361/202245629

Lister, T., Constantinescu, C., Ryan, W., Ryan, E., Gomez, E., Phillips, L., Rożek, A., Usher, H., Murphy, B. P., … Greenstreet, S. (2024). Long-term monitoring of Didymos with the LCOGT network and MRO after the DART impact. *Planet. Sci. J.*, *5*(5), 127. https://doi.org/10.3847/PSJ/ad4345

Lolachi, R., Glenar, D. A., Stubbs, T. J., and Kolokolova, L. (2023). Optical characterization of the DART impact plume: Importance of realistic ejecta scattering properties. *Planet. Sci. J.*, *4*(2), 24. https://doi.org/10.3847/PSJ/aca968

Michel, P., Cheng, A., Küppers, M., Pravec, P., Blum, J., Delbo, M., Green, S. F., Rosenblatt, P., Tsiganis, K., … Yu, Y. (2016). Science case for the Asteroid Impact Mission (AIM): A component of the Asteroid Impact & Deflection Assessment (AIDA) mission. *Adv. Space Res.*, *57*(12), 2529–2547. https://doi.org/10.1016/j.asr.2016.03.031

Michel, P., Küppers, M., Bagatin, A. C., Carry, B., Charnoz, S., de Leon, J., Fitzsimmons, A., Gordo, P., Green, S. F., … Carnelli, I. (2022). The ESA Hera mission: Detailed characterization of the DART impact outcome and of the binary asteroid (65803) Didymos. *Planet. Sci. J.*, *3*(7), 160. https://doi.org/10.3847/PSJ/ac6f52

Moreno, F., Campo Bagatin, A., Tancredi, G., Liu, P. Y., and Domínguez, B. (2022). Ground-based observability of Dimorphos DART impact ejecta: Photometric predictions. *Mon. Not. Roy. Astron. Soc.*, *515*(2), 2178–2187. https://doi.org/10.1093/mnras/stac1849

Moreno, F., Bagatin, A. C., Tancredi, G., Li, J.-Y., Rossi, A., Ferrari, F., Hirabayashi, M., Fahnestock, E., Maury, A., … Lin, Z.-Y. (2023). Characterization of the ejecta from the NASA/DART impact on Dimorphos: Observations and Monte Carlo Models. *Planet. Sci. J.*, *4*(8), 138. https://doi.org/10.3847/PSJ/ace827

Moreno, F., Tancredi, G., and Campo Bagatin, A. (2024). On the fate of slow boulders ejected after DART impact on Dimorphos. *Planet. Sci. J.*, *5*(3), 63. https://doi.org/10.3847/PSJ/ad26f8

Moskovitz, N., Thomas, C., Pravec, P., Lister, T., Polakis, T., Osip, D., Kareta, T., Rożek, A., Chesley, S. R., … Villa, K. (2024). Photometry of the Didymos system across the DART impact apparition. *Planet. Sci. J.*, *5*(2), 35. https://doi.org/10.3847/PSJ/ad0e74

Murphy, B. P., Opitom, C., Snodgrass, C., Knight, M. M., Li, J. Y., Chabot, N. L., Rivkin, A. S., Green, S. F., Guetzoyan, P., … de León, J. (2023). VLT/MUSE characterization of Dimorphos ejecta from the DART impact. *Planet. Sci. J.*, *4*(12), 238. https://doi.org/10.3847/PSJ/ad0a87

Naidu, S. P., Margot, J. L., Taylor, P. A., Nolan, M. C., Busch, M. W., Benner, L. A. M., Brozovic, M., Giorgini, J. D., Jao, J. S., and Magri, C. (2015). Radar imaging and characterization of the binary near-earth asteroid (185851) 2000 DP107. *Astron. J.*, *150*(2), 54. https://doi.org/10.1088/0004-6256/150/2/54

Ofek, E. O., Kushnir, D., Polishook, D., Waxman, E., Tohuvavohu, A., Ben-Ami, S., Katz, B., Gnat, O., Strotjohann, N. L., … Hershko, O. (2023). UV to near-IR observations of the DART-Dimorphos collision. *Mon. Not. Roy. Astron. Soc.*, *527*(4), 10507–10521. https://doi.org/10.1093/mnras/stad3707

Okawa, H., Arakawa, M., Yasui, M., Hasegawa, S., Toda, M., Shirai, K., and Yamamoto, Y. (2022). Effect of boulder size on ejecta velocity scaling law for cratering and its implication for formation of tiny asteroids. *Icarus*, *387*, 115212. https://doi.org/10.1016/j.icarus.2022.115212

O'Keefe, J. D., and Ahrens, T. J. (1977). Impact-induced energy partitioning, melting, and vaporization on terrestrial planets. In *Proceedings of the 8th Lunar Science Conference* (pp. 3357–3374). New York: Pergamon Press.

Opitom, C., Murphy, B., Snodgrass, C., Bagnulo, S., Green, S. F., Knight, M. M., de Léon, J., Li, J. Y., and Gardener, D. (2023). Morphology and spectral properties of the DART impact ejecta with VLT/MUSE. *Astron. Astrophys.*, *671*, L11. https://doi.org/10.1051/0004-6361/202345960

Poggiali, G., Brucato, J. R., Hasselmann, P. H., Ieva, S., Perna, D., Pajola, M., Lucchetti, A., Deshapriya, J. D. P., Della Corte, V., … Zanotti, G. (2022). Expected investigation of the (65803) Didymos–Dimorphos system using the RGB spectrophotometry data set from the LICIACube unit key explorer (LUKE) wide-angle camera. *Planet. Sci. J.*, *3*(7), 161. https://doi.org/10.3847/PSJ/ac76c4

Polishook, D., DeMeo, F. E., Burt, B. J., Thomas, C. A., Rivkin, A. S., Sanchez, J. A., and Reddy, V. (2023). Near-IR spectral observations of the Didymos system: Daily evolution before and after the DART impact indicates that Dimorphos originated from Didymos. *Planet. Sci. J.*, *4*(12), 229. https://doi.org/10.3847/PSJ/ad08ae

Pravec, P., Thomas, C. A., Rivkin, A. S., Scheirich, P., Moskovitz, N., Knight, M. M., Snodgrass, C., de León, J., Licandro, J., … Souami, D. (2022). Photometric observations of the binary near-earth asteroid (65803) Didymos in 2015−2021 prior to DART impact. *Planet. Sci. J.*, *3*(7), 175. https://doi.org/10.3847/PSJ/ac7be1

Raducan, S. D., Jutzi, M., Cheng, A. F., Zhang, Y., Barnouin, O., Collins, G. S., Daly, R. T., Davison, T. M., Ernst, C. M., … May, B. H. (2024). Physical properties of asteroid Dimorphos as derived from the DART impact. *Nat. Astron.*, *8*(4), 445–455. https://doi.org/10.1038/s41550-024-02200-3

Richardson, D. C., Agrusa, H. F., Barbee, B., Cueva, R. H., Ferrari, F., Jacobson, S. A., Makadia, R., Meyer, A. J., Michel, P., … Zannoni, M. (2024). The dynamical state of the Didymos system before and after the DART impact. *Planet. Sci. J.*, *5*(8), 182. https://doi.org/10.3847/PSJ/ad62f5

Rivkin, A. S., Chabot, N. L., Stickle, A. M., Thomas, C. A., Richardson, D. C., Barnouin, O., Fahnestock, E. G., Ernst, C. M., Cheng, A. F., … Hirabayashi, M. (2021). The Double Asteroid Redirection Test (DART): Planetary defense investigations and requirements. *Planet. Sci. J.*, *2*(5), 173. https://doi.org/10.3847/PSJ/ac063e

Roth, N. X., Milam, S. N., Remijan, A. J., Cordiner, M. A., Busch, M. W., Thomas, C. A., Rivkin, A. S., Moullet, A., Roush, T. L., … Hirabayashi, M. (2023). ALMA observations of the DART impact: Characterizing the ejecta at submillimeter wavelengths. *Planet. Sci. J.*, *4*(11), 206. https://doi.org/10.3847/PSJ/acfcaa

Rumpf, C. M., Lewis, H. G., and Atkinson, P. M. (2017). Asteroid impact effects and their immediate hazards for human populations. *Geophys. Res. Lett.*, *44*(8), 3433–3440. https://doi.org/10.1002/2017GL073191

Schmidt, N. (2019). Conceptualizing the asteroid threat and searching for a balanced answer between effectiveness and desirability. In N. Schmidt (Ed.), *Planetary Defense: Global Collaboration for Defending Earth from Asteroids and Comets* (pp. 217–230). Cham: Springer. https://doi.org/10.1007/978-3-030-01000-3_14

Shestakova, L., Serebryanskiy, A., and Aimanova, G. (2023). Observations of alkaline emissions NaI, KI and LiI during first minutes after DART probe impact on Dimorphos. *Icarus*, *401*, 115595. https://doi.org/10.1016/j.icarus.2023.115595

Tancredi, G., Liu, P. Y., Campo-Bagatin, A., Moreno, F., and Domínguez, B. (2023). Lofting of low-speed ejecta produced in the DART experiment and production of a dust cloud. *Mon. Not. Roy. Astron. Soc.*, *522*(2), 2403–2414. https://doi.org/10.1093/mnras/stac3258

Thomas, C. A., Naidu, S. P., Scheirich, P., Moskovitz, N. A., Pravec, P., Chesley, S. R., Rivkin, A. S., Osip, D. J., Lister, T. A., … Agrusa, H. F. (2023). Orbital period change of Dimorphos due to the DART kinetic impact. *Nature*, *616*(7957), 448–451. https://doi.org/10.1038/s41586-023-05805-2

Weaver, H. A., Sunshine, J. M., Ernst, C. M., Farnham, T. L., Mottola, S., Spencer, J. R., Marchi, S., Dello Russo, N., Barnouin, O., … DART Investigation Team. (2024). Lucy observations of the DART impact event. *Planet. Sci. J.*, *5*(2), 43. https://doi.org/10.3847/PSJ/ad1ee5

Wijayatunga, M. C., Armellin, R., Holt, H., Pirovano, L., and Lidtke, A. A. (2023). Design and guidance of a multi-active debris removal mission. *Astrodynamics*, *7*(4), 383–399. https://doi.org/10.1007/s42064-023-0159-3

Yu, Y., Michel, P., Schwartz, S. R., Naidu, S. P., and Benner, L. A. M. (2017). Ejecta cloud from the AIDA space project kinetic impact on the secondary of a binary asteroid: I. mechanical environment and dynamical model. *Icarus*, *282*, 313–325 https://doi.org/10.1016/j.icarus.2016.09.008